Increasing damage tolerance in composites using hierarchical brick-and-mortar microstructures

J. Henry, S. Pimenta*

Department of Mechanical Engineering, Imperial College London, South Kensington Campus, London, SW7 2AZ, UK

Abstract

Composites are attractive materials because of their high specific stiffness and specific strength, but their application in industry is restricted by their inherent lack of damage tolerance and stable energy dissipation mechanisms, due to the brittleness of the fibres. Nature overcomes a similar issue by arranging natural composites, made of mostly brittle constituents, in discontinuous and hierarchical microstructures. This work aims at evaluating the potential of hierarchical discontinuous carbon-fibre reinforced polymers to achieve damage tolerance, by a combination of modelling and experiments. Two different models (one analytical and the other numerical) are developed to predict the tensile response of hierarchical brick-and-mortar microstructures with two levels of hierarchies, and to design specimens with a non-linear response. Such specimens are then manufactured using laser micro-milled carbon/epoxy thin-plies, and tested under tension. The results show that the presence of discontinuities and hierarchies promotes stable energy dissipation before failure, ensures damage diffusion throughout the specimen, and delays damage localisation in otherwise brittle composites.

Keywords:
A. Crack Propagation and Arrest, A. Microstructure, C. Finite Element, C. Mechanical Testing, Carbon Fibre Reinforced Polymer

1. Introduction

Despite their high stiffness, high strength and their lightweight, conventional continuous-fibre composites suffer from a crucial lack of stable energy dissipation mechanisms, leading to over-designed structures and restricting the applications of composites. This is mainly due to the microstructure of conventional composites – with continuous stiff and brittle fibres embedded in a soft polymeric matrix – which promotes localisation of damage and leads to brittleness.

Although naturally-occurring composites (e.g. nacre, bone) are mostly composed by brittle constituents as well, Nature overcomes this inherent brittleness of conventional composites in two ways. Firstly, Nature uses discontinuous microstructures (Barthelat and Zhu, 2011, Rho et al., 1998, Menig et al., 2000), which proved to be essential to combine high stiffness, strength and toughness (Barthelat and Rabiei, 2011). Secondly, Nature uses hierarchies in the microstructure

*Corresponding author
Email addresses: joel.henry13@imperial.ac.uk (J. Henry), soraia.pimenta@imperial.ac.uk (S. Pimenta)

Henry J, Pimenta S (2018). Increasing damage tolerance in composites using hierarchical brick-and-mortar microstructures. *Journal of the Mechanics and Physics of Solids* 118, 332–340.DOI:10.1016/j.jmps.2018.06.003

of natural composites (up to seven levels in bone (Barthelat and Zhu, 2011, Zhang et al., 2011, Weiner and Wagner, 1998)), which is also crucial to achieve damage tolerance (Wei et al., 2015).

The fascinating and yet not fully-explained properties of natural composites (Mayer, 2005) motivated numerous attempts to model and mimic their microstructure and mechanical response. Gorbatikh et al. (2010) showed, with their model, that carefully engineered hierarchical microstructures (with different sizes of inclusions) could eliminate the stress concentrations at the larger inclusions, hence changing the failure mechanism to a more stable one. Experimentally, nacre-like synthetic composites achieved a 700-fold increase in the toughness of the brittle constituent (Mirkhalaf and Barthelat, 2015), and crack deflection capabilities (Narducci and Pinho, 2017). Other synthetic hierarchical discontinuous composites displayed damage diffusion, preventing catastrophic failure and increasing damage tolerance (Mirzaeifar et al., 2015).

Various methods have been developed to synthesise composites with bio-inspired hierarchical discontinuous microstructures, and have been classified by Mirkhalaf et al. (2016) in two categories. The "bottom-up" strategy creates the composite by assembling the different constituents together; this strategy includes, amongst others, multimaterial 3D printing (Mirzaeifar et al., 2015) which provides fast prototyping of samples, and polymer-coating process methods (Brandt et al., 2013) suitable for large-scale production. The second approach is the "top-down" strategy, in which an existing block of material is modified to create the discontinuities and hierarchies in the microstructure; this includes 3D laser engraving (Mirkhalaf and Barthelat, 2015) and laser micro-cutting of prepregs (Bullegas et al., 2016, Narducci and Pinho, 2017).

Unlike conventional composites, hierarchical discontinuous microstructures are more challenging to model, as they involve reinforcements of very different scales (Romanov et al., 2014, Dai and Mishnaevsky, 2014). Full Finite Element (FE) models and Molecular Dynamics Simulations have been considered (Xia et al., 2016) but, being computationally expensive, they are limited in the size of the Representative Volume Element (RVE) that they can study. This is also a problem for the Embedded Region (ER) technique, in which two independent FE meshes (representing host and embedded regions) are created and tied together (Romanov et al., 2014), allowing for instance to model carbon nanotubes within a polymeric matrix. Another solution is multi-scale FE models of RVEs (Piat and Schnack, 2003, Kanit et al., 2003, Pelissou et al., 2009, Mirkhalaf et al., 2016), where the homogenised mechanical properties of RVEs are calculated in smaller-scale FE models, and then applied as inputs to larger-scale FE models.

An alternative approach to model hierarchical discontinuous composites is to replace FE with simplified analytical methods, applied to an explicit representation of the microstructure (Pingle et al., 2008, Gorbatikh et al., 2010). For instance, Gorbatikh et al. (2010) developed a model for composites reinforced by inclusions with two very distinct sizes, which were modelled by rigid lines.

Another common way to model hierarchical materials is to view them as self-similar (Gao, 2006, Yao and Gao, 2007, Haghpanah et al., 2013) or quasi-self-similar (Zhang et al., 2011) microstructures. The self-similar assumption considers that all hierarchical levels of the microstructure are morphologically and mechanically similar, and differ only on the absolute value of a characteristic length; as a result, homogenised mechanical properties (e.g. strength, flaw tolerance) can be calculated by the same approach at all hierarchical levels (Gao, 2006, Pimenta

and Pinho, 2013, 2014). However, it has been shown (Zhang et al., 2011) that, in some cases, the assumption of self-similarity fails to correctly predict and mimic the mechanical response of hierarchical composites, even when their microstructure is morphologically self-similar.

This paper proposes, designs and demonstrates the potential of combining discontinuities and hierarchies in a microstructure, to promote stable energy dissipation mechanisms and achieve damage tolerance. This is achieved through modelling, manufacturing and testing of Hierarchical Brick-and-Mortar (HBaM) composites, which are realised through the "top-down" modification of (originally brittle) Carbon-Fibre Reinforced Polymers.

The paper is organised as follows: Sec. 2 proposes and compares two models (analytical and numerical) to predict the tensile response of HBaM composites, and designs microstructures to be manufactured and tested. Sec. 3 explains the experimental methods used for the manufacturing and the testing of the HBaM specimens. Sec. 4 presents the experimental results and discusses the potential of hierarchical discontinuous composites to achieve increased damage-tolerance. Finally, Sec. 5 draws the main conclusions of this work.

2. Design of hierarchical microstructures

2.1. Non-self-similar numerical model

2.1.1. Model definition

The model system studied in this work is a hierarchical brick-and mortar (HBaM) composite with two levels of hierarchy. Simple brick-and-mortar (BaM) microstructures are composed by bricks of one single size and, therefore, display a single level of hierarchy (with perfectly staggered bricks as shown in Fig. 1a); HBaM composites use the simple BaM microstructure (hereafter identified as level-0) as the building blocks of a larger BaM microstructure (hereafter identified as level-1), as shown in Fig. 1b. The lengths and thicknesses of level-0 and level-1 bricks are respectively l_0, t_0, l_1, t_1; the size of a level-1 brick can also be defined by the number of level-0 bricks it is made of ($n_x \times n_y$). The thickness of the mortar layer between bricks is t^{m} which, in this work, remains equal at both hierarchical levels. Tab. 1 describes the geometry of the HBaM microstructures used throughout this paper.

This HBaM microstructure was modelled *numerically*, with Finite Element (FE) simulations using the Abaqus software (Abaqus, 2013). The symmetries and the periodicity of the microstructure allow the entire material to be modelled by the unit-cell shown in Fig. 1c. The level-0 bricks are modelled using orthotropic linear-elastic plane-stress elements and Hashin failure criteria, with properties representative of a unidirectional carbon-epoxy thin ply (see Tab. 2). The mortar – hereafter designated as "matrix" – of both level-0 and level-1 is assumed to be created by an epoxy-rich interply region between the bricks, which is modelled using cohesive elements (see Tab. 2). The cuts defining the ends of the level-0 and level-1 bricks were represented by removing elements at the appropriate locations (see Fig. 1c). The structure was loaded in longitudinal tension by applying the boundary conditions shown in Fig. 1c.

It is important to notice that this numerical model does not assume self-similarity, as the unit-cell represents each level-0 "brick" of the microstructure explicitly, rather than homogenising the mechanical response of the level-0 BaM material within the level-1 bricks.

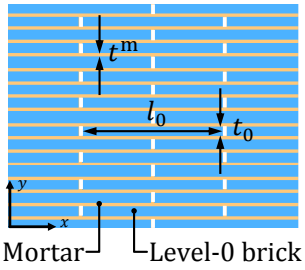

(a) BaM.

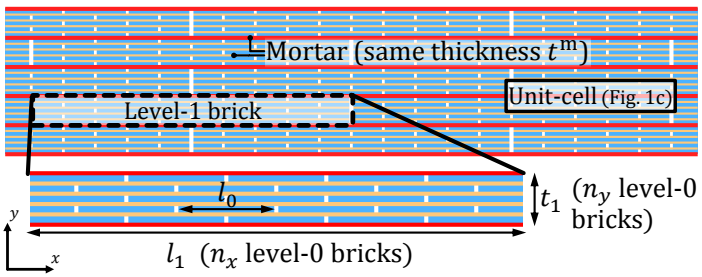

(b) HBaM: additional cuts are introduced to create level-1 brick-ends.

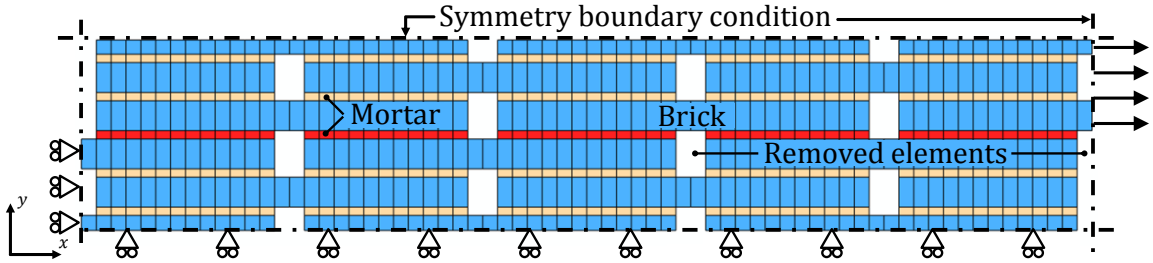

(c) Unit-cell of the numerical model for HBaM composites (zoom-in from (b)).

Figure 1: Microstructures of BaM and HBaM composites.

Table 1: Different microstructures considered in the design (Sec. 2) and testing (Sec. 4) of HBaM microstructures. Parameters n_x and n_y are defined in Fig. 1b.

	Microstructure	$l_0/l_{0\text{nom}}$	$t_0/t_{0\text{nom}}$	n_x	n_y
($l_{0\text{nom}} = 460$ µm, $t_{0\text{nom}} = t_{0\text{nom-a}} = 22$ µm)	*BaM-a*	1	1	1	1
Parametric study on geometry of level-0 bricks ($l_{0\text{nom}} = 460$ µm, $t_{0\text{nom}} = t_{0\text{nom-a}} = 22$ µm)	*Nominal-a*	1	1	5	5
	Short-a	1/2	1	5	5
	Long-a	2	1	5	5
	Scaled-up-a	2	2	5	5
Parametric study on geometry of level-1 bricks ($l_{0\text{nom}} = 460$ µm, $t_{0\text{nom}} = t_{0\text{nom-b}} = 28$ µm)	*Nominal-b*	1	1	5	5
	Thick-b	1	1	5	11
	Long-b	1	1	11	5
	Large-b	1	1	11	11

Table 2: Material properties of the carbon/epoxy thin ply prepreg used in the models and the experiments (Narducci and Pinho, 2017, Skyflex, 2015). Superscripts 'b', 'm', and 'p' refer to the 'brick', 'matrix', and 'ply' properties respectively. The two ply-thickness values correspond to two prepregs used experimentally, with two different fibre volume fractions. The longitudinal Young's modulus and strength of the bricks are calculated from values for the ply ($t^{p0} = 23$ µm, $E^{p0} = 102$ GPa, and $X^{p0} = 1892$ MPa (Narducci and Pinho, 2017)), using $E^b = E^{p0} \cdot t^{p0}/t_{0\text{nom}}$, and $X^b = X^{p0} \cdot t^{p0}/t_{0\text{nom}}$. The mode-I strength and toughness of the cohesive elements representing the matrix were set to unrealistically high values to mimic mode-II dominated failure.

Property	Variable	Unit	Set a	Set b
Prepreg ply thickness	t^p	µm	23	29
Level-0 brick thickness	$t_{0\text{nom}}$	µm	22	28
Thickness of the rich resin region between plies	t^m	µm	1	1
Fibre volume fraction in the ply	V_f	%	43	34
Longitudinal Young's modulus of the level-0 bricks	E^b	GPa	106.6	83.8
Longitudinal tensile strength of the level-0 bricks	X^b	MPa	1978	1554
Matrix mode II fracture toughness	$\mathcal{G}^m_{iic}$	kJ/m^2	0.90	0.90
Matrix shear strength	S^m	MPa	88.5	88.5

2.1.2. Mechanical response of HBaM composite

The tensile response observed in the numerical model of the HBaM microstructures is composed of three different stages, which are explained bellow and illustrated in Fig. 2 for the *nominal-a* microstructure (see Tab. 1):

i. *Linear–elastic stage* (up to point I in Fig. 2). This stage ends with damage initiation in the matrix, starting from the corners of neighbouring level-1 bricks (as shown by the stiffness degradation of the matrix in Fig. 2d, point I). Up to that point, the energy stored in the material is purely elastic, and there is no energy dissipated through damage (see Fig. 2b);

ii. *Damage accumulation stage* (between points I and III in Fig. 2). The longitudinal stresses in the bricks increase further (as shown by the stress fields in Fig. 2c, points II and III), but damage in the matrix propagates from the corners of level-1 bricks towards the centre of level-1 bricks, following the overlaps between level-0 bricks in a staircase pattern (as shown in Fig. 2d, points II and III). Consequently, the material loses tangent stiffness in an almost discrete way (see different slopes up to point I, between points I and II, and between points II and III in Fig. 2a), corresponding to damage propagation in each individual step of this staircase pattern. Moreover, Fig. 2b indicates that energy is being dissipated through damage of the matrix during this stage;

iii. *Post–failure stage* (after point III in Fig. 2). The maximum load–bearing capacity of the composite (at point III) is defined when a crack tip develops in the matrix (i.e. when damage equals 1 at the interface with the corners of neighbouring bricks); for the *nominal-a* geometry analysed in Fig. 2, this also corresponds to the moment when matrix damage within a level-1 brick creates a full rhombus shape. Subsequently, damage localises in one of the two level-1 bricks in the unit-cell (as shown in Fig. 2d, point IV), and the level-0 bricks unload elastically (as shown in Fig 2c, point IV).

The results from Fig. 2 show a high amount of energy dissipated stably through diffused damage and significant non-linearity in the overall stress-strain response of the HBaM composite, but one has to keep in mind that these results were obtained from a unit-cell model, which may not be representative of a full-scale specimen where damage could localise. To explore the possibility of damage localisation, a full scale HBaM composite specimen with 48 unit-cells was modelled as shown in Fig. 3, with no symmetry or periodicity imposed. Fig. 3a shows that the introduction of hierarchies prevents damage localisation: indeed, the rhombus shape of matrix damage found in the unit-cell model (Fig. 2d) is also observed throughout the full composite specimen, not only at the failure site (where the rhombus pattern is fully closed, leading to final failure of the composite), but also away from the failure site.

2.2. Self-similar analytical model

2.2.1. Model definition

An *analytical* model was also developed for the HBaM composite microstructures described in Sec. 2.1.1. However, unlike the numerical model detailed in Sec. 2.1.2, this analytical model uses the self-similar assumption which, for this particular microstructure, is defined as follows: bricks of each hierarchical level (level-0, level-1, ...) are assumed to have homogeneous material

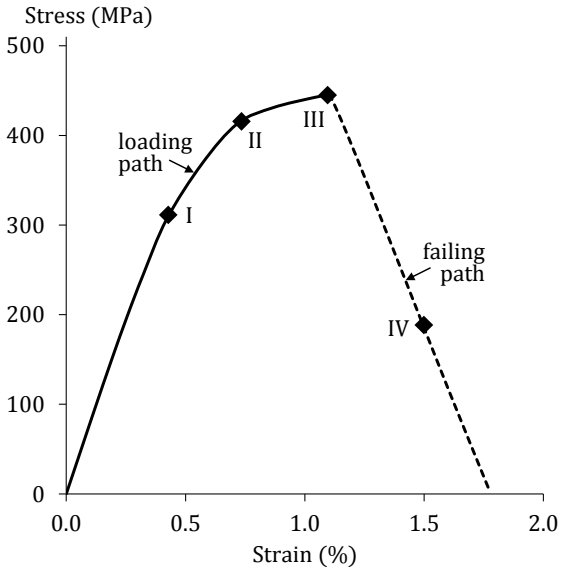

(a) Stress-Strain curve of the HBaM composite.

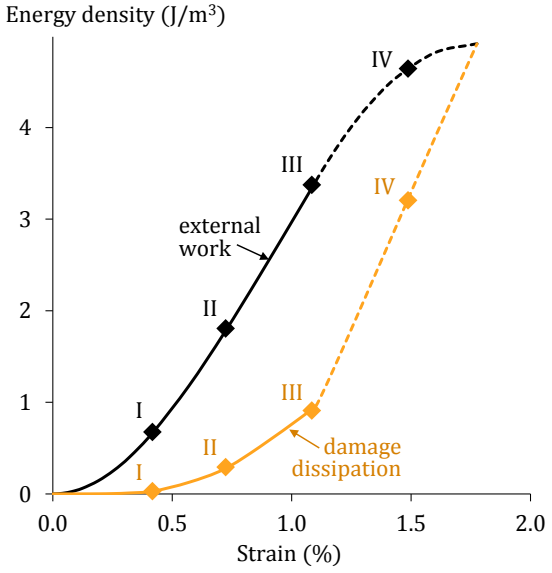

(b) Energy dissipation in the HBaM composite.

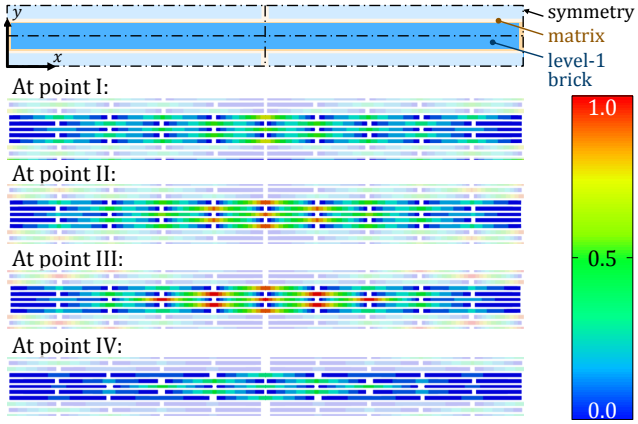

(c) Pattern of longitudinal tensile stresses in the level-0 bricks (normalised by the maximum value observed), mapped on 4 unit-cells for clarity.

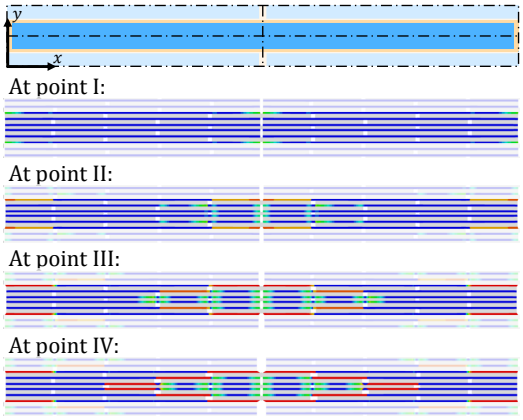

(d) Pattern of stiffness degradation in the matrix, mapped on 4 unit-cells for clarity.

Figure 2: Mechanical response of a HBaM composite (with a *nominal-a* microstructure, defined in Tab. 1), as predicted by a unit-cell numerical model.

properties, with a homogenised stress-strain response, and with a uniform response through the thickness of the brick.

The analytical self-similar model predicts the response of the level-0 BaM microstructure using a shear-lag approach for simple BaM composites with linear-elastic bricks and bilinear matrix response (Pimenta and Robinson, 2014). Subsequently, the non-linear stress-strain curve of the level-0 BaM microstructure is approximated by a piecewise linear curve, and is used as the input for the brick material response of the BaM structure of level-1; this required extending the existing formulation for linear-elastic bricks (Pimenta and Robinson, 2014, Henry and Pimenta, 2018) to non-linear elastic bricks (see App. A). Therefore, assuming that the level-0 bricks have a linear elastic response, the model is used recursively to calculate the homogenised stress-strain responses of the different hierarchical levels of a HBaM microstructure.

(a) In a HBaM virtual specimen, matrix damage is dispersed in all level-1 bricks, throughout the entire microstructure.

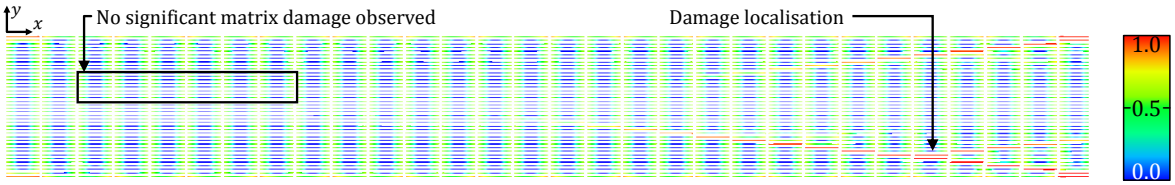

(b) In a BaM virtual specimen, matrix damage localises (on the right) and is not diffused throughout the microstructure.

Figure 3: Stiffness degradation of the matrix in BaM and HBaM virtual specimens.

2.2.2. Comparison of numerical and analytical models

The results of the analytical model for HBaM composites with two hierarchical levels are compared to the numerical results in Fig. 4, for different brick geometries (described in Tab. 1). Although the trend for how the initial stiffness of a HBaM composite changes with different level-0 brick geometries seems to be correctly captured by the analytical model (Fig. 4), the loss of tangential stiffness due do damage dissipation is not well predicted by the analytical model, whose results present very little non-linearity compared to the numerical model. Since the same material properties and constitutive laws were used in both models, this suggests that the analytical model is not able to account for the progressive damage propagation within each level-1 brick. Therefore, the analytical model cannot correctly calculate the stress-strain response of HBaM composites, and becomes progressively more inaccurate as the level-0 bricks become shorter (Fig. 4a), and as level-1 bricks become thicker and larger (Fig. 4b).

The results of Fig. 4 show the limitation of the self-similar assumption, as it neglects that the real failure mechanism in HBaM composites (as predicted by the numerical model) requires the interaction between the different hierarchical levels: the level-1 brick-ends trigger stress-concentrations in the neighbouring level-1 bricks, initiating damage in the matrix which propagates between the level-0 bricks. Moreover, the assumption of self-similarity implies a uniform stress through the thickness of the bricks of all levels (compare the stress fields calculated by the analytical model (Fig. 5a) and by the numerical model (Fig. 5b)); although this seems acceptable for level-0 bricks, Fig. 5b shows that the stress fields in the level-1 bricks is complex and not uniform through the thickness. Therefore, the remaining of this work will use the numerical model (although computationally more expensive) to investigate the behaviour of HBaM composites.

2.3. Optimisation of the HBaM microstructure

Intuitively, Sec. 2.1.2 suggests the existence of an optimal microstructure for HBaM composites, to maximize the non-linearity of the stress-strain curve and the stable energy dissipation through damage diffusion. Let us first explore how the geometry of the level-0 bricks affects the response of HBaM composites (i) qualitatively, looking at the failure mechanisms (Fig. 6), and

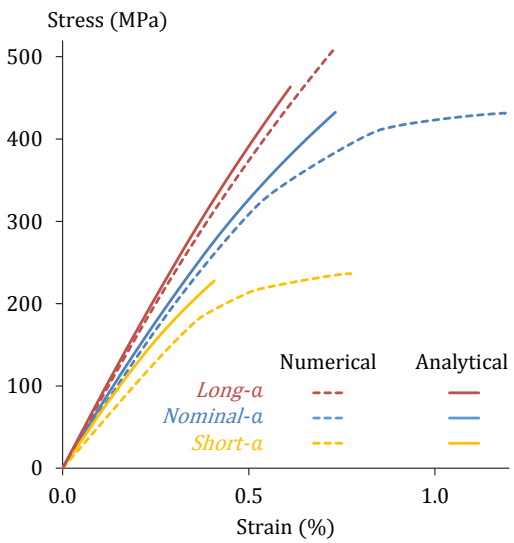

(a) Stress-strain curves for different geometries of the level-0 bricks.

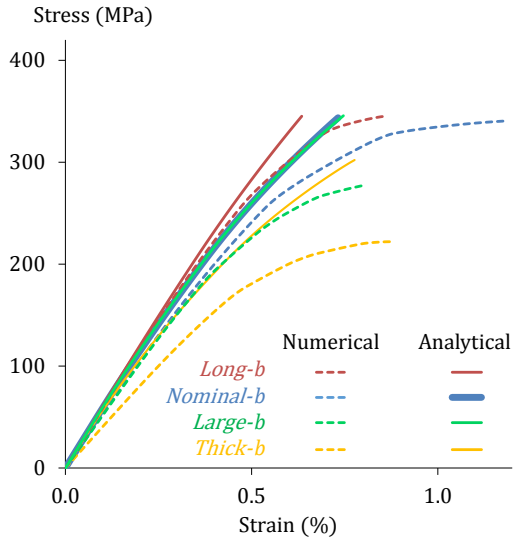

(b) Stress-strain curves for different geometries of the level-1 bricks.

Figure 4: Comparison of the stress-strain curves predicted by the analytical model (using the self-similar assumption) against the numerical model, for HBaM composites with two levels and geometries defined in Tab. 1. The stress fields for the *nominal-a* microstructure are shown in Fig. 5.

(a) Analytical model.

(b) Numerical model.

Figure 5: Tensile stress fields within a level-1 brick calculated by the analytical and numerical models, for the *nominal-a* microstructure. The colour scale is normalised to the maximum stress reached in the numerical model.

(ii) quantitatively, looking at the stress-strain curves and the energy dissipated (Fig. 7). This will be done by comparing the response of HBaM composites with different level-0 brick geometries against the *nominal-a* microstructure (as specified in Tab. 1), while keeping the number of level-0 bricks in each level-1 brick unchanged (to preserve the rhombus shape of matrix damage):

- Increasing the length of level-0 bricks (Fig. 6b) leads to fracture of the level-0 bricks and, consequently, premature and brittle failure of the HBaM composite, leading to a quasi-linear response (see *long-a* in Fig. 7a) and very little damage energy dissipated (see *long-a* in Fig. 7b);
- However, decreasing the length of level-0 bricks (Fig. 6c) leads to a decrease in the stiffness and the strength of the HBaM composite (see *short-a* in Fig. 7a), as the shear-lag stress transfer becomes less effective. Consequently, although the ratio of damage to elastic energy remains the same as in the *nominal-a* case, the absolute value of both energies is reduced in the *short-a* microstructure (see *short-a* in Fig. 7b);
- Scaling-up both the length and the thickness of level-0 bricks (Fig. 6d) increases the energy release rate for delamination between the bricks, and triggers premature unstable failure of the overlaps between bricks (Pimenta and Robinson, 2014). Therefore, the stress-strain curve of the HBaM composite will stop before the maximum non-linear stage is reached (compare *scaled-up-a* and *nominal-a* in Fig. 7a), and less energy will be dissipated through diffuse damage of the matrix (see *scaled-up-a* in Fig. 7b). This agrees with existing literature, which stresses the importance of using small-scale building blocks in hierarchical structures (Currey, 1977, Gao et al., 2003, Mishnaevsky, 2011).

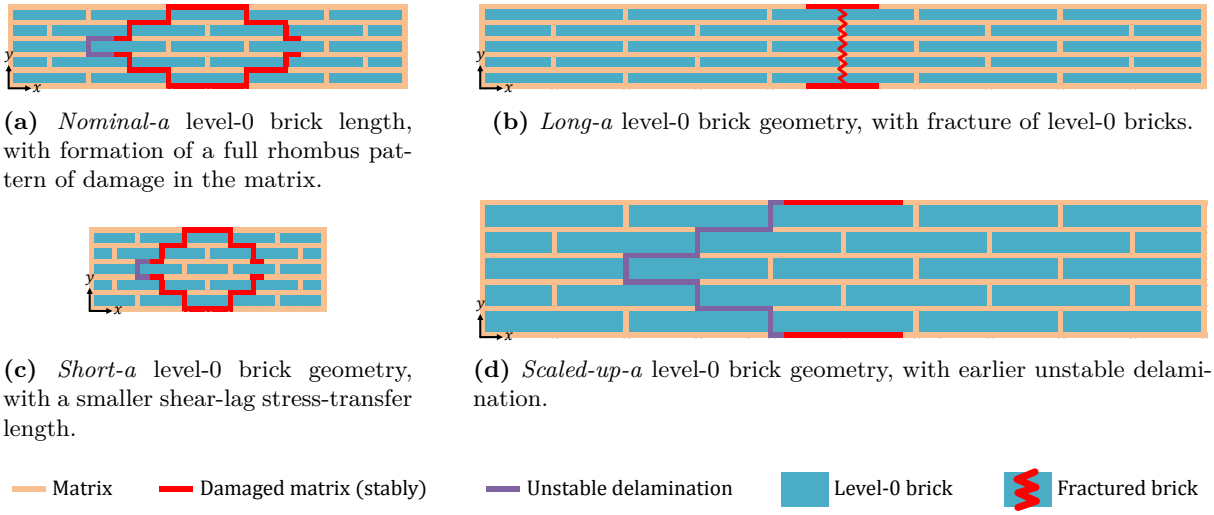

(a) *Nominal-a* level-0 brick length, with formation of a full rhombus pattern of damage in the matrix.

(b) *Long-a* level-0 brick geometry, with fracture of level-0 bricks.

(c) *Short-a* level-0 brick geometry, with a smaller shear-lag stress-transfer length.

(d) *Scaled-up-a* level-0 brick geometry, with earlier unstable delamination.

Figure 6: Effect of the geometry of level-0 bricks on the failure mechanism of a level-1 brick in HBaM composites.

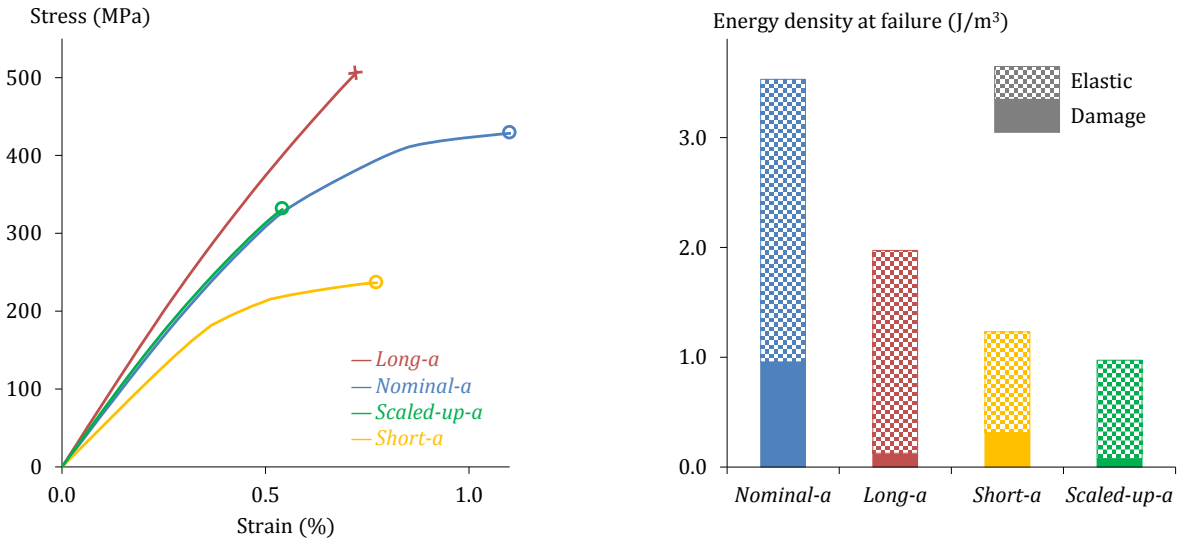

(a) Stress-strain curves. Final failure modes: matrix delamination (○), level-0 brick fracture (×).

(b) Internal energy at the point of maximum stress.

Figure 7: Mechanical response calculated by the numerical model for HBaM composites with different geometries of level-0 bricks.

Let us now investigate how the geometry of the level-1 bricks affects the response of the HBaM composite (i) qualitatively, looking at the failure mechanisms (Fig. 8), and (ii) quantitatively, looking at the stress-strain curves and the energy dissipated (Fig. 9). This will be done by comparing the response of HBaM with different level-1 brick geometries (achieved by changing the number of level-0 bricks inside a level-1 brick) against the *nominal-b* microstructure (as specified in Tab. 1), while keeping the size of level-0 bricks unchanged:

- When the length of level-1 bricks is increased (i.e. when n_x increases, see Fig. 8b), both the failure mechanism (i.e. damage of the matrix along a rhombus pattern) and the strength of the HBaM composite remain unchanged; however, only the matrix nearer the centre (horizontally) of each level-1 brick is affected by damage degradation, as the rhombus pattern of damage does not reach the ends of the level-1 bricks; this yields little strain at failure (see *long-b* in Fig. 9a) and much less damage energy dissipated (see *long-b* in Fig. 9b) than for the *nominal-b* level-1 brick length;

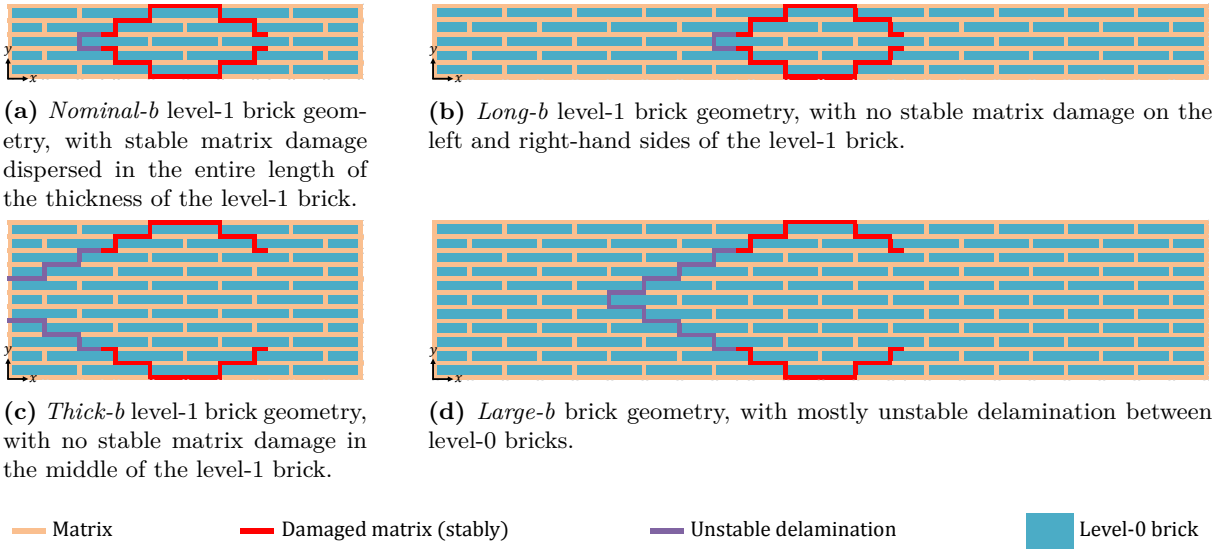

(a) *Nominal-b* level-1 brick geometry, with stable matrix damage dispersed in the entire length of the thickness of the level-1 brick.

(b) *Long-b* level-1 brick geometry, with no stable matrix damage on the left and right-hand sides of the level-1 brick.

(c) *Thick-b* level-1 brick geometry, with no stable matrix damage in the middle of the level-1 brick.

(d) *Large-b* brick geometry, with mostly unstable delamination between level-0 bricks.

Figure 8: Effect of the geometry of level-1 bricks on the failure mechanism of HBaM composites.

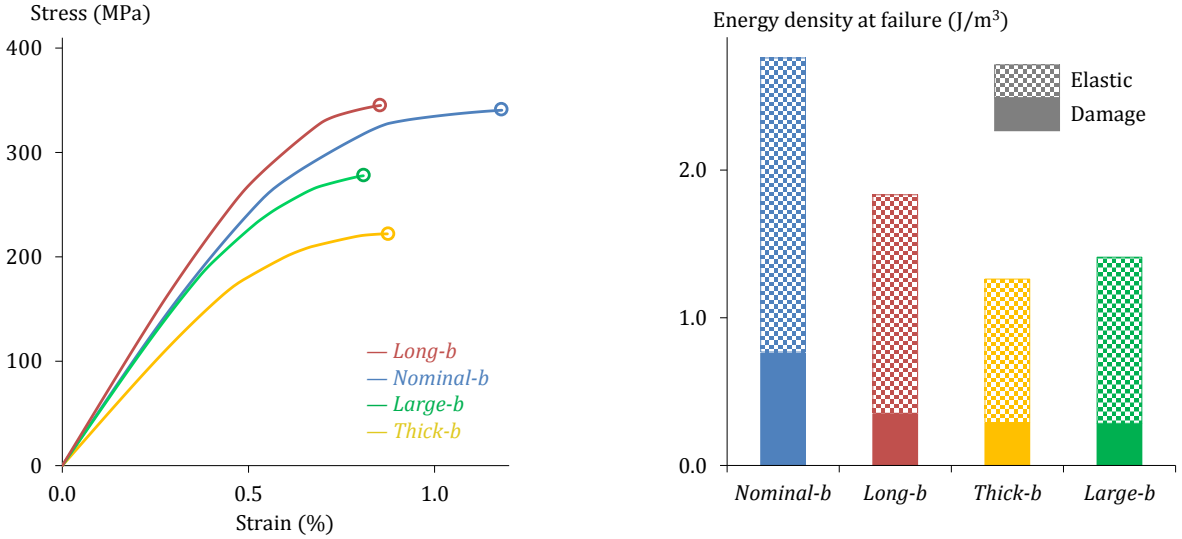

(a) Stress-strain curves. Failure mode: matrix delamination (○).

(b) Internal energy at the point of maximum stress.

Figure 9: Mechanical response calculated by the numerical model for HBaM composites with different geometries of level-1 bricks.

- When the thickness of level-1 bricks is increased (i.e. when n_y increases, see Fig. 8c), the middle (vertically) of each level-1 brick is not loaded, and therefore the stiffness and the strength of the HBaM composite are reduced (see *thick-b* in Fig. 9a). As the rhombus damage pattern cannot fully close within one level-1 brick (as it reaches the vertical boundary with the neighbouring bricks), less energy is dissipated stably through damage (see *thick-b* in Fig. 9b) than for the *nominal-b* level-1 brick thickness;

- When both the length and the thickness of the level-1 bricks are scaled-up (i.e. both n_x and n_y increase, see Fig. 8d), the length of the rhombus damage pattern reaches a critical size above which the delamination propagates unstably, yielding premature failure of the level-1 brick (compare *large-b* to *nominal-b* in Fig. 9a). Moreover, the ratio of debonded-matrix-length to level-1 brick-area is smaller than for the *nominal-b* geometry, and therefore the energy dissipated by matrix damage is reduced (see *large-b* in Fig. 9b).

2.4. Comparison of BaM and HBaM composites

Let us now compare the *nominal-a* HBaM microstructure with the *BaM-a* architecture. As already mentioned in Sec. 2.1, Fig. 3a suggests that energy is dissipated through matrix damage throughout the entire virtual specimen when hierarchies are used. On the contrary, for a simple BaM virtual specimen of the same size, Fig. 3b suggests that the regions with significant matrix damage are localised at a few brick interfaces only, and damage propagates unstably in a specific region of the material, causing catastrophic failure of the composite specimen with no significant accumulation of damage away from the failure site. These different patterns of matrix damage suggest that HBaM composites do not suffer from damage localisation, unlike BaM composites.

Quantitatively, the energy dissipated through damage by the HBaM microstructure is two times higher than that of the BaM equivalent. Moreover, the energy dissipated through damage represents only 9% of the total energy for BaM composites, against 27% for the HBaM composites.

3. Experimental method

3.1. Material properties

All microstructures identified in Tab. 1 (except *scaled-up-a*) have been manufactured using SkyFlex USN020A carbon/epoxy prepregs, whose properties are given in Tab. 2. Note that the thicknesses of the plies used for the parametric studies of the level-0 brick geometry ($t_{0\mathrm{nom-a}}$) and of the level-1 brick geometry ($t_{0\mathrm{nom-b}}$) are different, because the plies were cut from two different rolls (see Tab. 2).

3.2. Manufacturing plates and specimens with HBaM microstructures

The hierarchical microstructures identified in Sec. 2 were manufactured using the following process (Bullegas et al., 2016):

a. The discontinuities in the HBaM microstructures were laser-cut in thin CFRP prepreg plies using a Diode Pumped Solid State (DPSS) micromachining system, which provided sufficient accuracy for the microstructures to be manufactured (Narducci and Pinho, 2017). The cuts were introduced perpendicularly to the fibre direction in each prepreg ply, according to the patterns shown in Figs. 10b and 10c, to create the brick-ends. Two patterns of cuts (A and C, as shown in Fig. 10c) were required to manufacture a simple BaM microstructure (in which the cuts generated the end of the level-0 bricks); to create the ends of the level-1 bricks in the HBaM microstructures, two additional patterns of cuts (B and D shown in Fig. 10c) were required.

b. In order to achieve high precision in the through-the-thickness alignment of the laser-cut patterns in the microstructure, alignment holes were also laser-cut from the prepreg plies. The plies with the laser-cut patterns were then laid-up as shown in Fig. 10 and as specified in Tab. 3, using the alignment holes along with an alignment rig with pins (used to keep the same reference frame for all plies (Bullegas et al., 2016)) to align the patterns of cuts as accurately as possible. This created uncured plates with HBaM microstructures (see Fig. 10a).

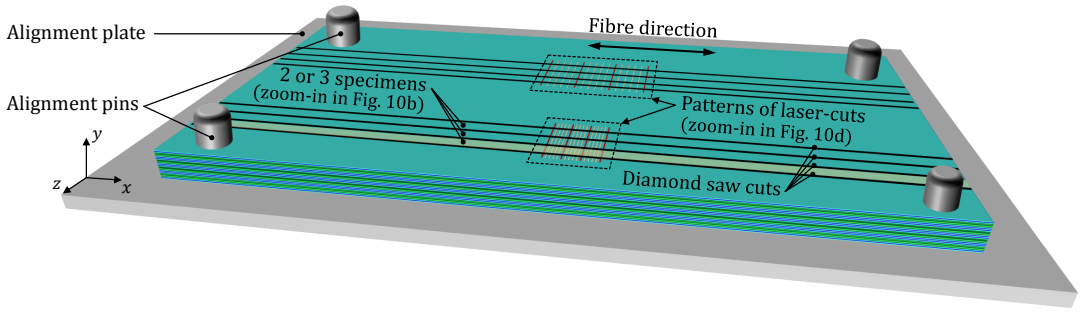

(a) Lay-up and alignment of the prepreg plies using the alignment rig (not to scale).

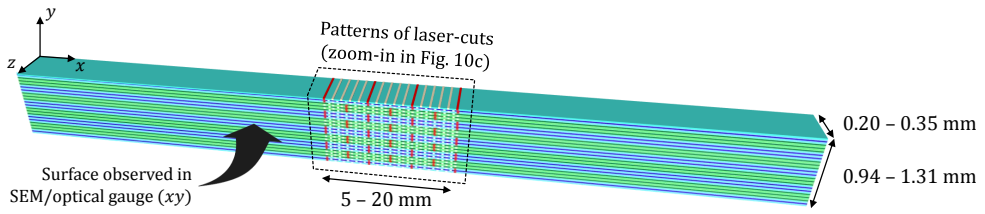

(b) Overview of one HBaM specimen (not to scale).

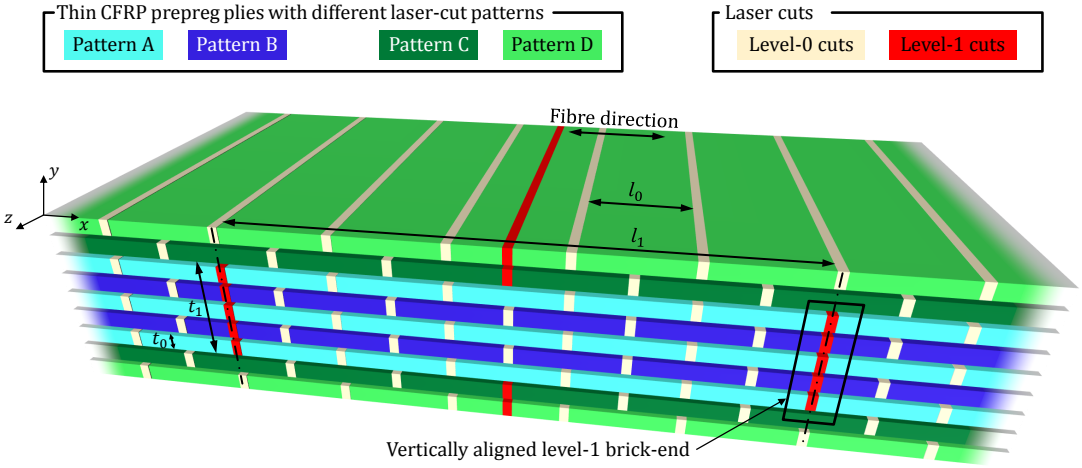

(c) Level-1 brick of a *Nominal-a* HBaM microstructure, manufactured with thin plies with four different laser-cut patterns (not to scale). The layup sequence shown here is $DC(ABABA)CD$ (the complete layup sequence is given in Tab. 3).

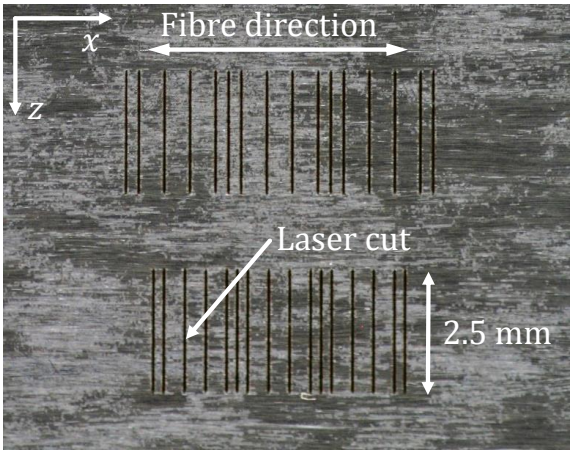

(d) Hierarchical patterns of laser-cuts in a thin prepreg ply.

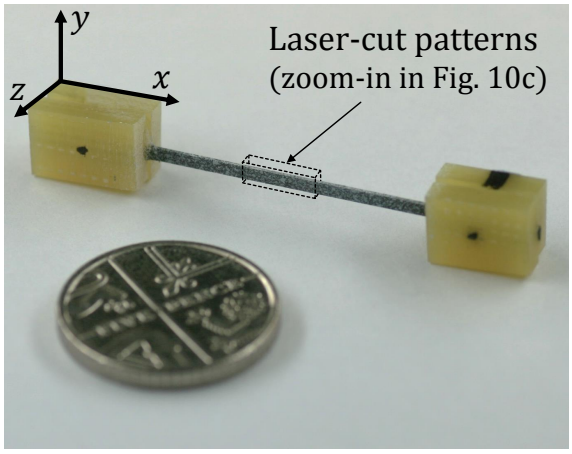

(e) End-tabbed specimen. The hierarchical microstructure is in the centre of the specimen, facing the z-direction.

Figure 10: Manufacturing process of HBaM composites.

Table 3: Layup sequence for each microstructure manufactured.

Microstructure	Number of plies through the thickness	Layup sequence (see Sec. 3.2 and Fig. 10c)	Plate thickness (mm)
BaM-a	41	$(AC)_{20}A$	0.94
Nominal-a	41	$(ABA)[(CDCDC)(ABABA)]_3(CDCDC)(ABA)$	0.94
Short-a	41	$(ABA)[(CDCDC)(ABABA)]_3(CDCDC)(ABA)$	0.94
Long-a	41	$(ABA)[(CDCDC)(ABABA)]_3(CDCDC)(ABA)$	0.94
Nominal-b	41	$(ABA)[(CDCDC)(ABABA)]_3(CDCDC)(ABA)$	1.19
Thick-b	45	$([BA]_3)([CD]_5C)([AB]_5A)([CD]_5C)([AB]_3)$	1.31
Long-b	41	$(ABA)[(CDCDC)(ABABA)]_3(CDCDC)(ABA)$	1.19
Large-b	45	$([BA]_3)([CD]_5C)([AB]_5A)([CD]_5C)([AB]_3)$	1.31

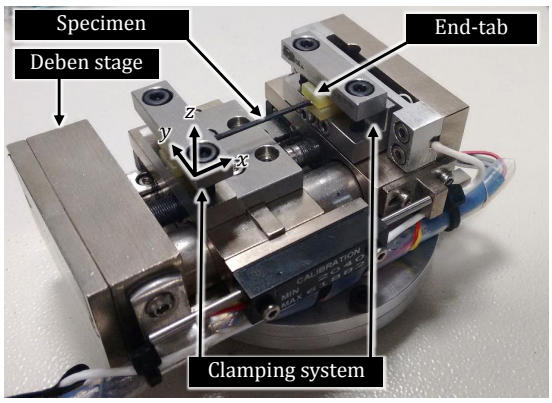

(a) HBaM specimen in the Deben tensile stage.

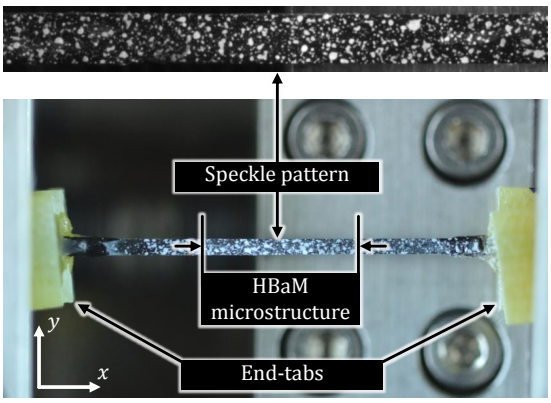

(b) Speckle pattern on a clamped HBaM specimen.

Figure 11: Tensile testing set-up used in the experiments.

c. The plates with the HBaM microstructures were cured in an autoclave, according to the temperature and pressure cycle specified by the manufacturer (Skyflex, 2015).

Once the plates were cured, specimens were cut to a $0.20 - 0.35$ mm width (defined in the z-direction, see Fig. 10a), using a high-precision diamond saw. The length of the laser-cut pattern (2.5 mm also defined in the z-direction, see Fig. 10d) ensured that at least two specimens with a hierarchical microstructure throughout their entire z-direction could be cut out of each pattern of laser-cuts. The specimens were then end-tabbed using glass/epoxy plates (Fig. 10e). The dimensions of the specimens, given in Tab. 3 and Fig. 10b, were chosen to ensure that failure occurred before the testing rig reached its maximum load capacity (Sec. 3.3).

It will be shown in Sec. 4.3 that the alignment rig described above in Point b allowed us to obtain an accuracy in the relative placement of the laser-cut patterns better than 50 µm. Nevertheless, the manual lay-up process still induced small shifts of the plies relatively to the perfectly-aligned lay-up idealised in Sec. 2. The magnitude of the ply-shifts and their effect on the mechanical response of the HBaM specimens manufactured will be discussed in Sec. 4.3.

3.3. Testing method

For each HBaM microstructure, one set of specimens was tested in the SEM, to observe the damage and failure mechanisms occurring during tensile loading. Those specimens were polished

using grinding papers and a diamond suspension on polishing cloths, and gold-coated, to ensure good-quality SEM pictures. Another set of specimens was sprayed with a speckle pattern and tested using an optical strain gauge (iMetrum, 2018), to accurately measure their stress-strain response (Fig. 11b).

The two sets of specimens were both tested in tension using a Deben in-situ MT300 tensile stage (Deben, 2013) (see Fig. 11a). The specimens were tested under displacement control, at a speed rate of 0.1 mm/min to ensure quasi-static conditions. The maximum permissible load in the Deben stage is 300 N.

4. Results

4.1. Damage tolerance in HBaM composites

4.1.1. Damage diffusion in the microstructure

Fig. 12a reveals diffused damage formed during tensile loading of a HBaM specimen, observed as opening of the ends of level-1 bricks. This pattern of damage was observed throughout the entire microstructures of the HBaM specimens (i.e. not only at the failure site, but also away from the failure site).

The diffuse damage pattern observed in the HBaM microstructure (Fig. 12a) was not seen in the non-hierarchical BaM composite specimens, demonstrating that the diffusion of damage throughout the specimen is triggered by the use of hierarchical microstructures. This supports the numerical results from Sec. 2.4, which predict twice as much damage energy dissipation in the HBaM specimens, compared to the non-hierarchical ones. This also corroborates experimental results from the literature (Brandt et al., 2013, Mirzaeifar et al., 2015), which observed diffused damage in hierarchical microstructures.

Different mechanisms where found to contribute to stable energy dissipation before final failure of the specimens (see Fig. 13):

- *Matrix/interface failure* (Figs. 13a and 13b): this is the main mechanism for which the microstructure was developed and designed. Matrix (Fig. 13a) and interface (Fig. 13b) failure occurred between level-0 bricks, either following the rhombus pattern predicted by numerical models (see Sec. 2.1.2 and Fig. 2d), but also in other smaller brick overlaps created by random ply-shifts which occurred during the lay-up process (to be discussed in Sec. 4.3).

- *Fibre breakage*: due to the stochastic nature of the strength of the fibres and to the occurrence of random ply shifts (to be discussed in Sec. 4.3), some fibres failed in the experimental specimens, although this was not predicted by the numerical model (Fig. 13c). This fibre breakage not only dissipates some energy directly, but it also triggers further energy dissipation through failure of the matrix/interface (as mentioned in the previous point) and pull-out of fibre-ends (as will be explained in the next point);

- *Fibre pull-out*: at relatively high strains (i.e. close to final failure of the specimen), broken fibres and pre-cut brick-ends started to pull out (Fig. 13d), hence dissipating energy through friction with the surrounding material.

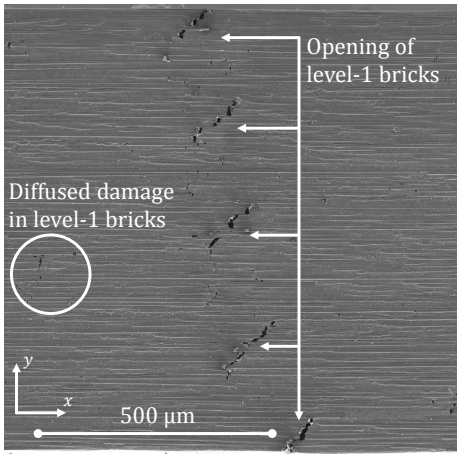

(a) Diffused damage at 89% of the maximum load.

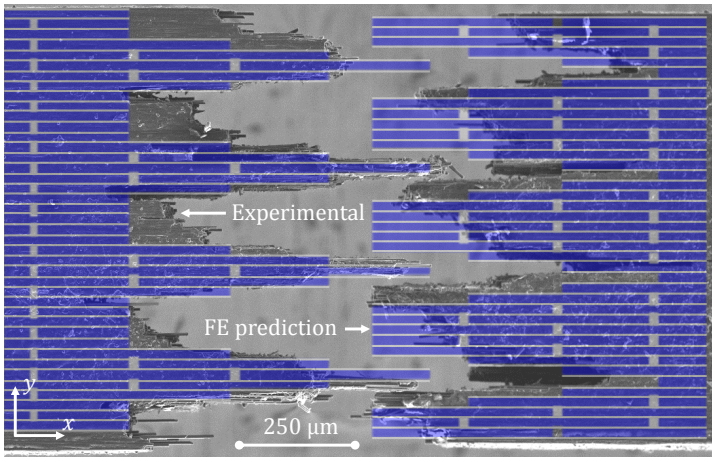

(b) Comparison between the fracture surfaces observed experimentally and predicted by the numerical model.

Figure 12: Diffuse damage and fracture surfaces in representative HBaM specimens, observed in the experiments and predicted by the numerical model.

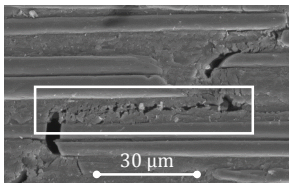

(a) Matrix failure.

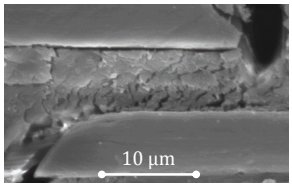

(b) Matrix/fibre interface failure.

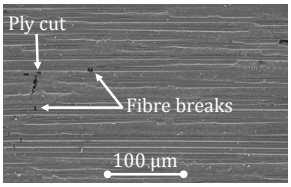

(c) Fibre breaks.

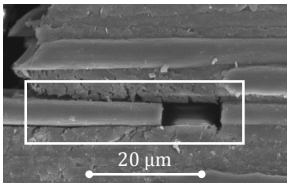

(d) Fibre pull out.

Figure 13: Diffused damage mechanisms observed in the SEM in HBaM specimens before final failure.

Fig. 12b shows an overall good agreement between the fracture surfaces predicted by the numerical model and observed experimentally, as the rhombus staircase pattern of damage at the interface between level-0 bricks, predicted in Sec. 2.1.2, is also seen in the experiments. Nevertheless, small discrepancies between the fracture surfaces predicted by the numerical model and observed experimentally can be noticed in Fig. 12b; this is due to small random shifts between the CFRP plies, which occurred during the lay-up process, as will be discussed in Sec. 4.3.

4.1.2. Non-linear stress-strain response of HBaM microstructures

The experimentally-measured stress-strain responses of three *nominal-a* specimens are compared against the prediction of the numerical model in Fig. 14a. In both cases, non-linearity is observed, but the experimental specimens failed prematurely in comparison with the simulated specimen; moreover, the experimental specimen was also stiffer than predicted by the model. Random ply-shifts were hypothesised to be the main responsible for these deviations, as will be discussed in Sec. 4.3.

In order to ensure that the non-linearity observed in the global stress-strain curve of specimens (as shown in Fig. 14a) was due to uniformly large strains in the entire gauge length of a specimen (rather than due to large strains localised at a small portion of the gauge length), strains were also measured in three distinct sub-regions of the gauge length of a specimen. Fig. 14b shows that the amount of non-linearity in the experimental stress-strain curves is simi-

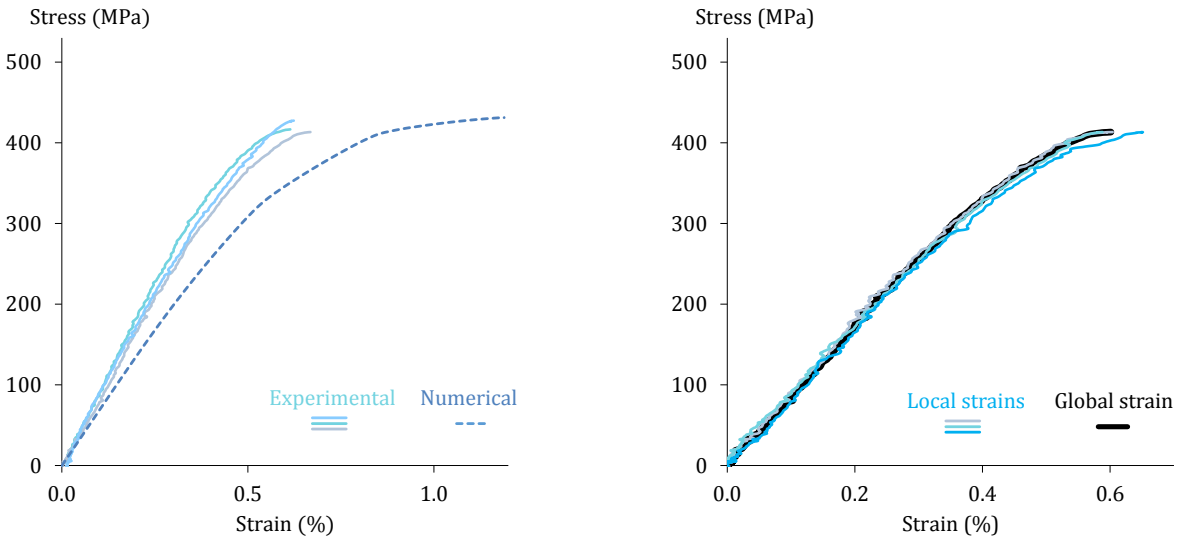

(a) Stress-strain curves predicted by the numerical virtual specimen compared against those obtained experimentally with three nominally identical specimens.

(b) Local (from 3 strain gauges) and global (from 1 strain gauge) stress-strain responses of one single HBaM specimen.

Figure 14: Stress-strain response of *nominal-a* HBaM specimens.

lar in all sub-regions within a specimen, including the sub-region of final specimen failure as well as the sub-regions away from the failure site. This corroborates the results from Fig. 3a, predicting diffuse damage (and, consequently, stress-strain non-linearity) across the entire HBaM specimen.

4.2. Parametric study of HBaM microstructures

Figs. 15a-15c show the effect of level-0 brick length on the fracture surface of HBaM experimental specimens. Figs. 15a-15b show that, below the *nominal-a* level-0 brick length, the fracture surface of HBaM specimens still follows the rhombus pattern of matrix damage predicted by the numerical model (as identified in Fig. 6a), with limited fibre-breakage; however, the effect of random ply-shifts (which occurred during manufacturing, see Sec. 4.3) on the fracture surface becomes more evident as the level-0 brick length decreases, which leads to a less well-defined HBaM pattern in the fracture surface of the *short-a* microstructure (Fig. 15a), when compared to that of the *nominal-a* specimen (Fig. 15b).

As the level-0 brick length increases to sufficiently large values to cause extensive brick failure (as shown in Fig. 15c), the fracture surface of HBaM specimens becomes more chaotic, although some features of the rhombus pattern of matrix damage predicted by the numerical model for shorter level-0 bricks are still visible. The mismatch between the fracture surfaces of the *long-a* microstructure observed experimentally (in Fig. 15c) and predicted numerically (in Fig. 6b) is likely due to the stochastic variability of the strength of the individual fibres, which makes some level-0 bricks able to withstand higher loads than those predicted by the (deterministic) numerical model; these statistically stronger level-0 bricks were then able to fail by debonding and pull-out rather than tensile brick failure.

For non-hierarchical BaM microstructures, the fracture surface of each specimen followed a different random pattern across each specimen (see example in Fig. 15d), as expected. While the fracture surface of the *BaM* specimens is also dominated by debonding between level-0 bricks

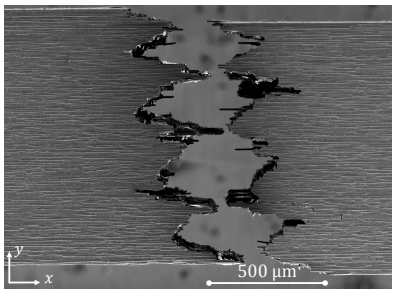

(a) *Short-a* specimen.

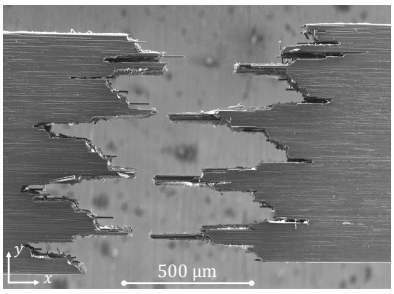

(b) *Nominal-a* specimen.

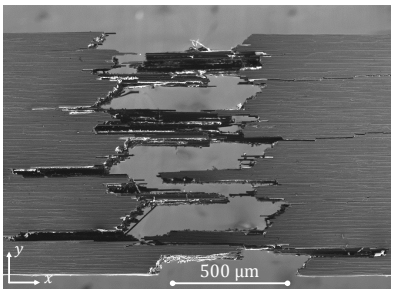

(c) *Long-a* specimen.

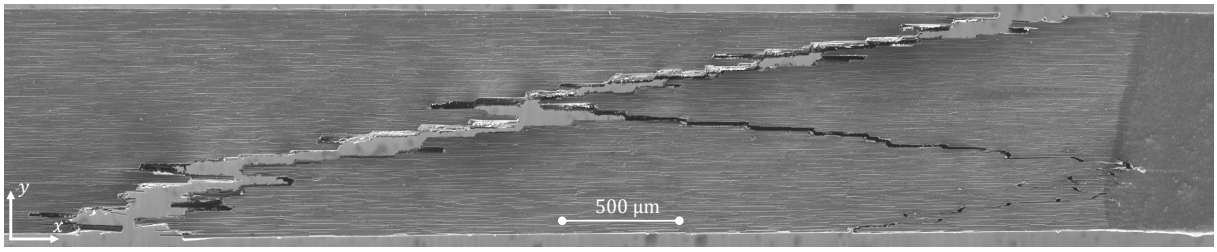

(d) *BaM-a* specimen.

Figure 15: Experimental fracture surfaces of specimens used in the parametric study of the level-0 brick geometry.

along a staircase pattern, the damage accumulation mechanism is significantly different from that observed in the HBaM *nominal-a* specimen, and the former does not evidence the same pattern of damage accumulation away from the final fracture surface as observed at the failure site.

Fig. 16 summarises the influence of the dimensions of level-1 bricks on the fracture surface and stress-strain curve of HBaM specimens. The fracture surfaces of *large-b* (Fig. 16a) and *thick-b* (Fig. 16b) specimens agree very well with the numerical predictions (shown in Figs. 8d and 8c respectively). The relative trends between the stress-strain curves predicted by the numerical models for the different level-1 brick geometries are also observed in the experimental results (see Fig. 16d). The quantitative discrepancies between the experimental and numerical stress-strain curves, as well as the differences between the observed (Fig. 16c) and predicted (Fig. 8b) fracture surfaces of *long-b* specimens, are believed to be due to random ply-shifts, which will be discussed in Sec. 4.3.

4.3. Effect of ply-shifts

Throughout Secs. 4.1 and 4.2, it has been hypothesised that random ply-shifts occurred during the lay-up process (due to the finite tolerance between the diameter of the alignment pins and the diameter of the laser-cut ply holes, see Fig. 10a), and that these ply-shifts are one of the main reasons for the differences observed between the numerical and the experimental results, both in terms of fracture surfaces and stress-strain curves.

To verify this hypothesis, SEM pictures of specimens in which the opening of brick-ends was clear (such as Fig. 12a) were used to estimate the shift (in the x-direction) between (i) the experimentally-observed position of the level-1 brick-ends (which, in Fig. 12a, are not vertically aligned) and (ii) the expected position of the level-1 brick-ends (which, as shown in Fig. 10c, should be vertically aligned, both within a level-1 brick and throughout the thickness of the specimen). The resulting shift measured within a level-1 *nominal-a* brick within Fig. 12a is

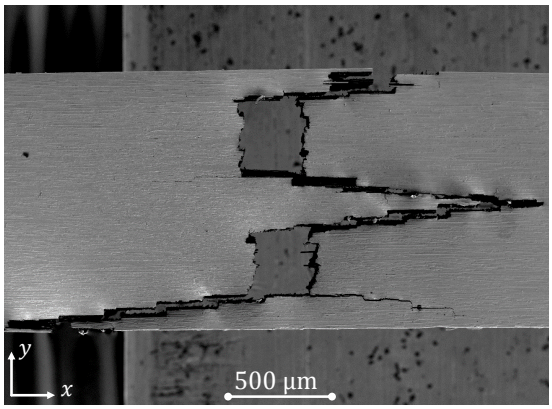

(a) Fracture surface of a *large-b* specimen.

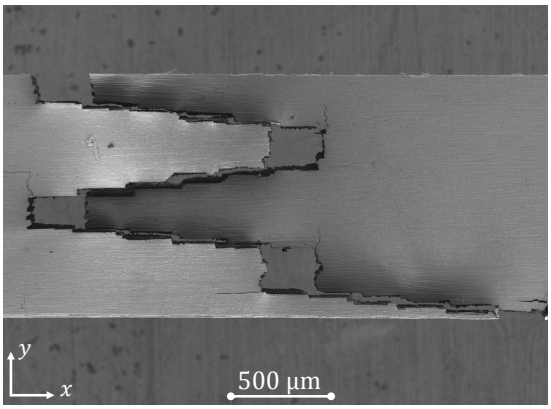

(b) Fracture surface of a *thick-b* specimen.

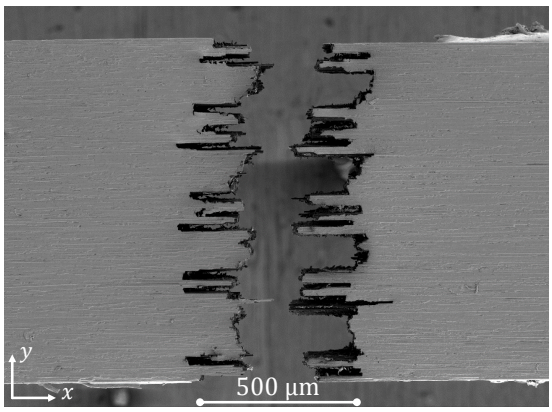

(c) Fracture surface of a *long-b* specimen.

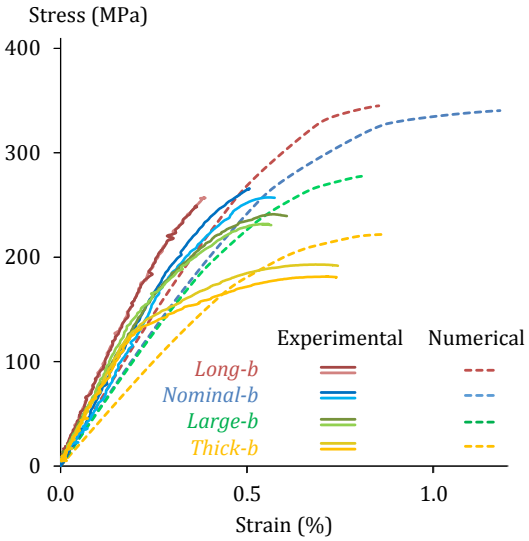

(d) Stress-strain curves of the HBaM microstructures with different level-1 brick geometries.

Figure 16: Fracture surfaces and stress-strain curves of HBaM with different level-1 brick-geometries. *Nominal-b* specimens had a similar fracture surface as the *nominal-a* specimens (shown in Fig. 15b).

illustrated in Fig. 17b; a similar process was carried out for other HBaM specimens, as shown in Fig. 17a and Fig. 17c.

This quantification of ply-shifts revealed that the *thick-b* (Fig. 17a) and *large-b* specimens had the smallest amount of ply-shifts of all specimens analysed. Interestingly, these specimens also showed the best agreement between experimental results and model predictions, both in terms of (i) fracture surfaces (compare Figs. 8c vs. 16b, and 8d vs. 16a), and (ii) the strains at failure (Fig. 16d).

Assuming that the shift of a ply remains uniform along the whole ply length (x-axis) and depth (z-axis), the measured ply-shifts were then introduced in the numerical models for the specimens which were most affected by ply-shifts. The fracture surfaces predicted by the modified numerical models compare extremely well with the experiments (see Figs. 18a, 18b, and 18c).

Fig. 19a shows that accounting for ply-shifts in the numerical model of the *nominal-b* specimens would reduce the predicted failure strain down to the value observed experimentally. These results suggest that ply-shifts are responsible for a significant loss of stress-strain nonlinearity and, therefore, energy dissipation. This also explains why natural composites tend

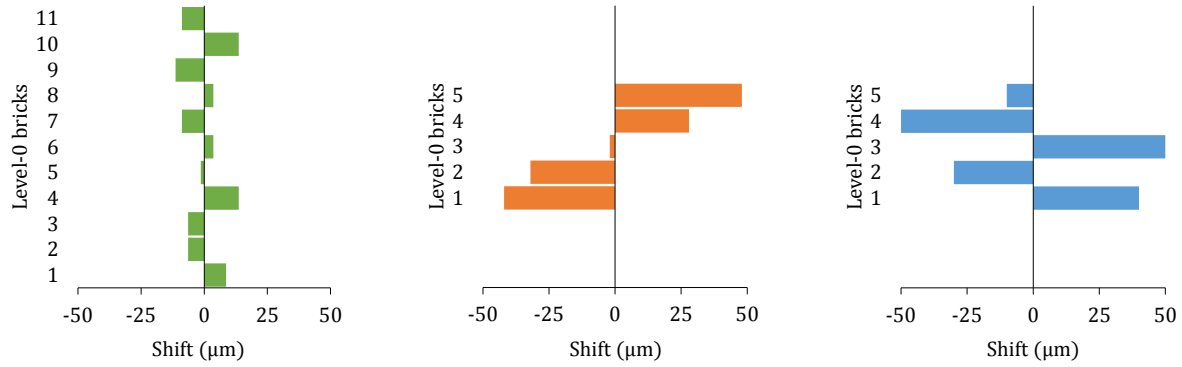

(a) *Thick-b* specimen. **(b)** *Nominal-a* specimen. **(c)** *Long-b* specimen.

Figure 17: Ply-shifts of each of the level-0 bricks in a level-1 brick, for different microstructures.

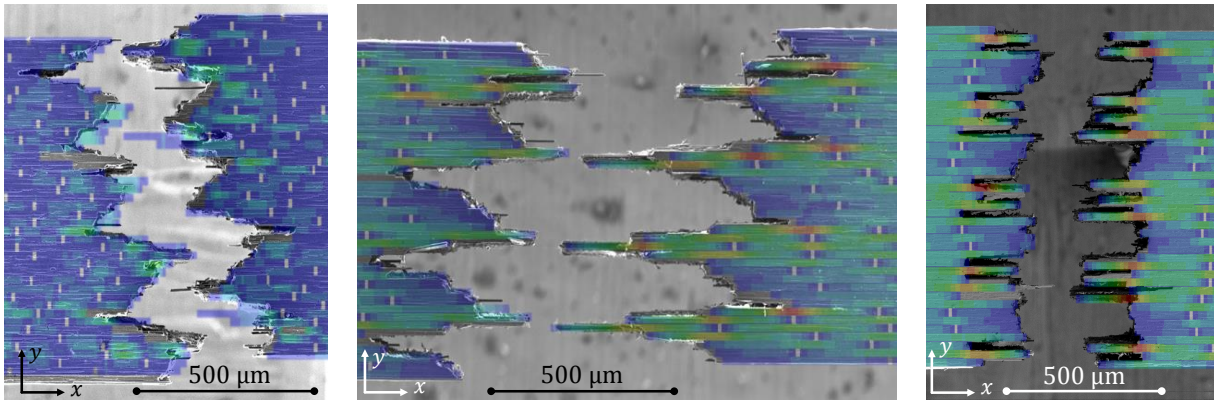

(a) *Short-a* specimen. **(b)** *Nominal-a* specimen. **(c)** *Long-b* specimen.

Figure 18: Fracture surfaces of HBaM specimens, as observed in the experiments and predicted by the numerical model considering ply-shifts.

to have perfectly staggered microstructures (rather than microstructures with random shifts), as it maximises their ability to dissipate energy before failure and, consequently, their damage tolerance (Lei et al., 2012).

Fig. 19b shows the effect that the ply-shifts measured in the *nominal-a* specimen would have had in the different BaM microstructures. Let us first compare the effect of ply-shifts on BaM and HBaM microstructures: for the same ply-shifts, the strength of BaM composites is reduced by 22% compared with the perfectly-staggered microstructure, while only by 7% for the *nominal-a* HBaM, suggesting that the addition of hierarchies reduces the dependence of the strength on the level of alignment. This is because ply-shifts in level-0 bricks reduce the overlap length between neighbouring bricks and trigger an even earlier damage localisation in the BaM microstructure, hence considerably diminishing the strength; however, for HBaM composites, despite ply-shifts in level-0 bricks, matrix failure still has to follow a rhombus pattern (which, for the *nominal-a* microstructure, contains the interface along three consecutive bricks) before final failure, which explains why most of the strength is maintained.

The strength reduction observed with ply-shifts in the simple BaM microstructure agrees with previous works from the literature (Abid et al., 2018, Henry and Pimenta, 2017b, Zhang et al., 2010); these studies concluded that randomness and statistical variations in the overlap length between fibres and platelets would trigger the localisation of damage, therefore lowering

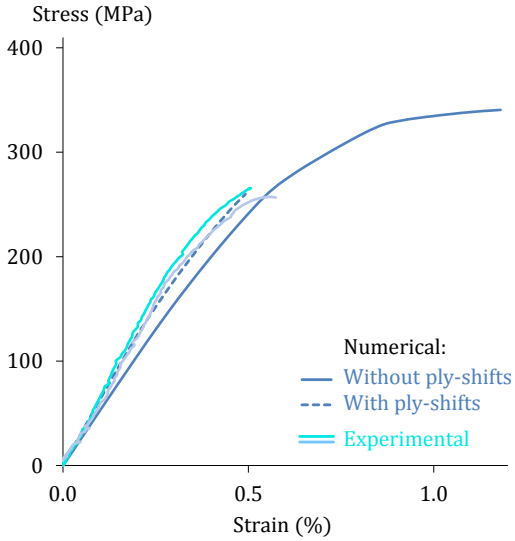

(a) Stress-strain curves of the *nominal-b* specimens measured experimentally, and predicted numerically with and without accounting for ply-shifts.

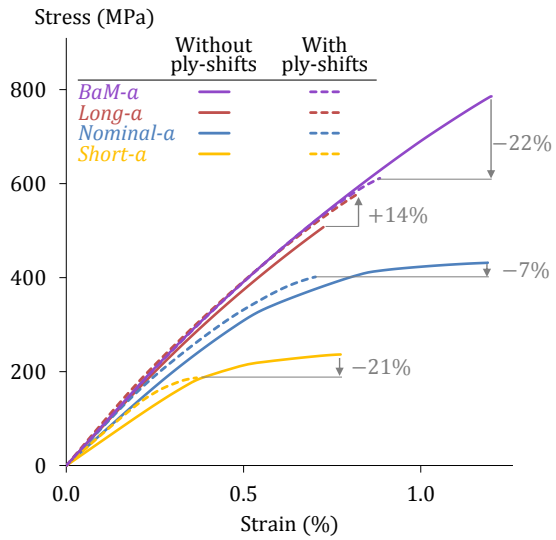

(b) Stress-strain curves for different geometries of the level-0 bricks, with and without considering the effect of the ply-shifts shown in Fig. 17b.

Figure 19: Effect of ply-shifts on the stress-strain curves of HBaM composites.

the strength (up to 40%), the ductility and energy absorption of discontinuous composites; however, the present study suggests that HBaM microstructures can delay this localisation of damage.

Let us now look at how varying the length of level-0 bricks modifies the effect of ply-shifts (see Fig. 19b). Failure of microstructures *nominal-a* and *short-a* is governed by brick debonding and pull-out, and both microstructures are weakened by the presence of ply-shifts. However, the *short-a* microstructure exhibits a strength reduction of 22% when ply-shifts are considered, compared to the perfectly-staggered case, while the strength reduction for the *nominal-a* specimens is only 7%. This is because *short-a* specimens have shorter level-0 bricks, and therefore the same absolute value of ply-shifts as in the *nominal-a* microstructure will have a stronger relative effect in *short-a* specimens.

On the contrary, the strength of the *long-a* microstructure improves by 14% with the presence of ply-shifts. This improvement occurs because the *long-a* microstructure fails when level-0 bricks fracture under tension, as a result of the stress concentrations due to the ends of the neighbouring level-0 bricks; in the perfectly-staggered microstructure, these level-0 brick-ends are aligned at the same location, which maximises the total stress concentration at the middle of a brick. Consequently, ply-shifts eliminate the perfect alignment of neighbouring brick-ends, hence reducing the stress concentrations at the middle of a level-0 brick, and allowing for a higher strength to be reached by specimens dominated by tensile failure of level-0 bricks (Fig. 19b).

Optimal HBaM microstructures can still be designed even if the alignment of the microstructure is subjected to variability (as observed with the present manufacturing process). To achieve this optimal design, level-0 bricks should be slightly longer than the ones designed for perfectly aligned microstructures, in order to increase the shortest overlap length between neighbouring bricks.

5. Conclusions

In this work, hierarchical brick-and-mortar composites with two levels of hierarchy have been designed, manufactured and tested. The following conclusions can be reached:

- Although the microstructure of a HBaM composite is self-similar (with two morphologically identical hierarchical levels), the assumption of self-similarity cannot be used to accurately calculate the mechanical response of the composite, as the failure mechanism involves an interaction between the two hierarchical scales: failure initiation is triggered in the composite via features *at the larger scale*, while propagation occurs via damage in the matrix following a rhombus pattern *in the smaller scale*. Moreover, the stress fields also vary within a given level of hierarchy.
- The hierarchical microstructure ensures that damage initiates and propagates throughout the entire specimen before damage localisation, hence promoting (i) *non-linearity*, providing a warning before failure, and (ii) *stable energy dissipation* via diffused damage throughout the material before failure (which was quantified by numerical simulations, and verified qualitatively in experiments).
- The HBaM microstructure can be optimised by tailoring both the aspect-ratio and the absolute dimensions of the bricks, at each hierarchical level. These parameters are governed by different mechanisms at each scale:
  - At the *smaller scale*: (i) the brick aspect-ratio is selected to maximise the force carried and transmitted between the level-0 bricks, while preventing fracture of the bricks; (ii) the brick absolute thickness should be minimised, in order to ensure stable and diffused delamination of the bricks, instead of localising damage due to premature delamination.
  - At the *larger scale*: (i) the brick aspect-ratio is selected to ensure that the rhombus pattern of matrix damage can fully develop, while maximising the efficiency of each level-1 brick to dissipate energy; (ii) the absolute brick dimensions are selected in order to avoid both damage localisation (which will occur if the level-1 bricks are too small), and unstable damage propagation (which will occur if the level-1 bricks are too large).
- Ply-shifts created during the manufacturing process have different effects on different level-0 brick geometries. On the one hand, ply-shifts reduce the overlap length between bricks, which triggers premature final failure of HBaM microstructures with relatively short level-0 bricks. On the other hand, ply-shifts reduce the stress concentrations due to brick-ends, which will delay final failure of HBaM microstructure with relatively long level-0 bricks. Moreover, random ply-shifts also stiffen HBaM microstructures. Therefore, ply-shifts have to be accounted for when optimising the microstructure of hierarchical discontinuous materials.

Compared to non-hierarchical BaM microstructures, it was shown that HBaM microstructures (i) dissipate more energy stably before failure, (ii) present a more non-linear response, (iii) delay damage localisation further, and (iv) are less sensitive to microstructural imperfections such as ply-shifts. Consequently, this study shows that combining discontinuous and hierarchical features in the microstructure of a composite can make it more tolerant to defects and damage.

Acknowledgements

S. Pimenta acknowledges the support from the Royal Academy of Engineering in the scope of her Research Fellowship on 'Multiscale discontinuous composites for large scale and sustainable structural applications' (2015-2019). The authors are also grateful to Steve Harrison from Triple-H Composites for supplying the prepreg material used in this work.

Appendices

A. Extension of the brick-and-mortar model for non-linear-elastic bricks

The aim of this section is to summarise how an existing model for single-level BaM composites with hybrid brick types (Pimenta and Robinson, 2014, Henry and Pimenta, 2017a, 2018) was extended for non-linear-elastic bricks, as mentioned in Sec. 2.2.

The current model considers a composite with perfectly staggered bricks (see Fig. A.1a, and zoom on the unit-cell in Fig. A.1b). The matrix has a bilinear response in shear (with material properties showed in Tab. 2), and the bricks have a non-linear response in tension; both responses are approximated by piecewise-linear stress-strain curves, as exemplified in Fig. A.1c for the matrix, and in Fig. A.1d for the bricks.

According to a 1-dimensional shear-lag mechanism (in which there are no through-the-thickness stress gradients within a brick or matrix layer), the matrix will transfer shear-stresses between each pair of neighbouring bricks, along the overlap between brick-ends. Along each brick, tensile stress will therefore increase from the brick-ends (where the stress is set to zero) to the centre of the brick (where the stress is maximum), as shown in Fig. A.1b. This non-homogeneous stress state in the bricks, combined with their piecewise non-linear tensile response, means that different *segments* of one brick along the overlap will have different tangent stiffnesses (as exemplified in Fig. A.1b).

The brick half-overlap shown in Fig. A.1b (of length L) can be regarded as a series of 4 segments; let us for example focus on Segment 2. In Segment 2, brick $\mathcal{A}$ is in Subdomain 1 (with tangent stiffness E_1 and stress $\sigma_{\mathcal{A}}(\varepsilon_{\mathcal{A}}) = E_1 \cdot \varepsilon_{\mathcal{A}} + \sigma_1^0$), brick $\mathcal{B}$ is in Subdomain 2 (with tangent stiffness E_2 and stress $\sigma_{\mathcal{B}}(\varepsilon_{\mathcal{B}}) = E_2 \cdot \varepsilon_{\mathcal{B}} + \sigma_2^0$), and the matrix is in Subdomain 1 (with tangent stiffness G_1^{m}). Using a method similar to the one developed for hybrid bricks (Henry and Pimenta, 2017a) yields the following governing differential equation for the shear-lag stress transfer in Segment 2 in Fig. A.1b:

$$
\begin{aligned}
&\frac{d^2\Psi(x)}{dx^2} = \operatorname{sign}\left[G_1^{\mathrm{m}}(\gamma)\cdot\tilde{E}_{12}\right]\cdot\lambda_{12}^2\cdot\Psi(x),\\
&\text{where}\begin{cases}
\lambda_{12} &= \sqrt{\dfrac{2}{T\cdot t^{\mathrm{m}}}\cdot\left|\dfrac{G_1^{\mathrm{m}}(\gamma)}{\tilde{E}_{12}}\right|},\\
\Psi(x) &= \Delta\sigma(x) + \dfrac{\sigma^{\infty}\cdot\Delta E_{21} - \sigma_2^0\cdot E_1 + \sigma_1^0\cdot E_2}{\bar{E}_{12}},\\
\Sigma E_{12} &= E_1 + E_2,\\
\Delta E_{21} &= E_1 - E_2,\\
\bar{E}_{12} &= \Sigma E_{12}/2,\\
\tilde{E}_{12} &= \dfrac{2\cdot E_1\cdot E_2}{E_1+E_2},
\end{cases}
\end{aligned}
\tag{A.1}
$$

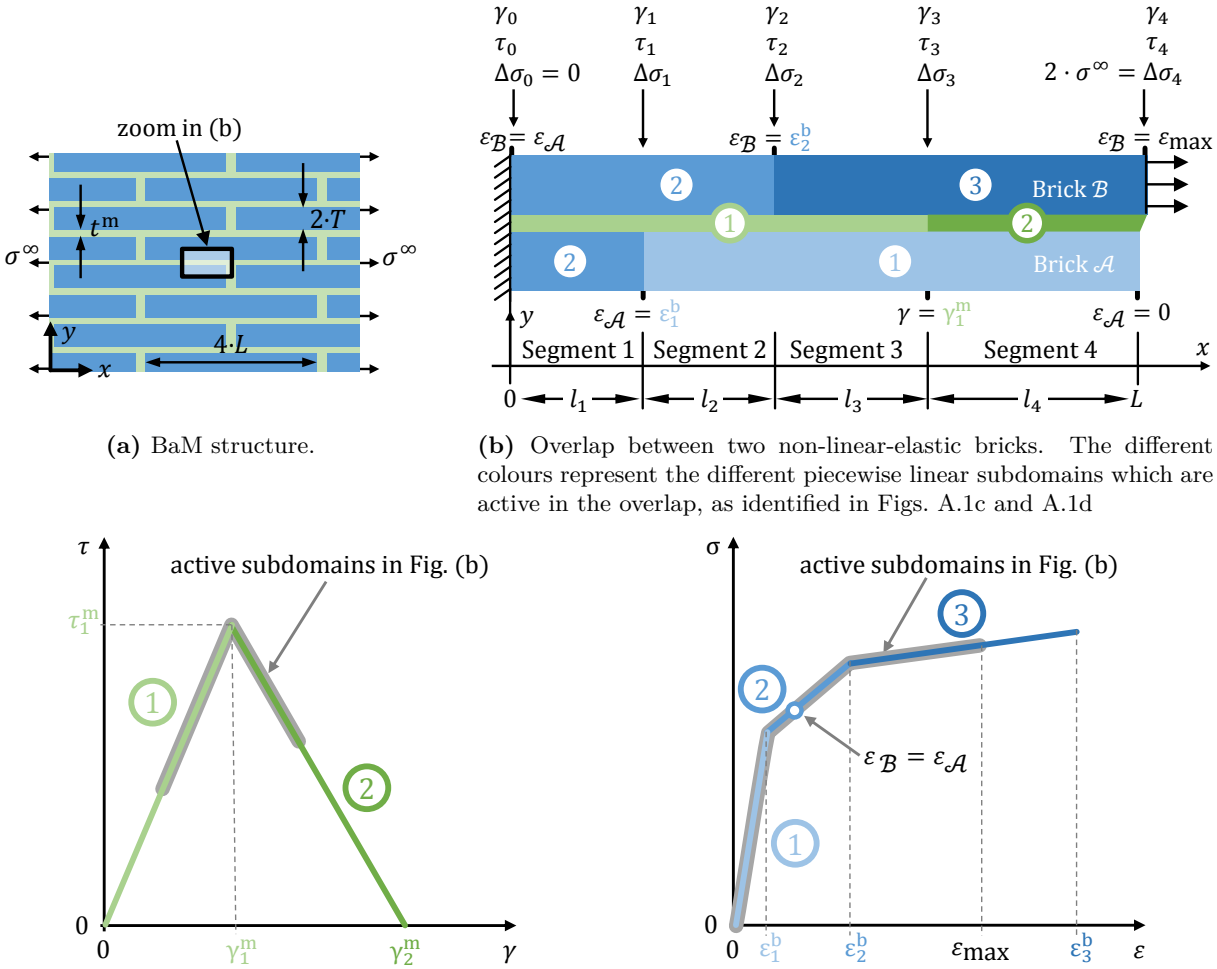

(a) BaM structure.

(b) Overlap between two non-linear-elastic bricks. The different colours represent the different piecewise linear subdomains which are active in the overlap, as identified in Figs. A.1c and A.1d

(c) Example of a matrix piecewise-linear constitutive law (with 2 subdomains).

(d) Example of a brick piecewise-linear constitutive law (with 3 load-bearing subdomains).

Figure A.1: Overview of the extension of the hybrid BaM model (Henry and Pimenta (2018)) to BaM composites with non-linear-elastic bricks.

and where $\Delta\sigma(x)$ is the stress difference $\sigma_{\mathcal{B}}(x) - \sigma_{\mathcal{A}}(x)$ along the overlap.

For each Segment $k = \{1, 2, 3, 4\}$ in the overlap in Fig. A.1b, an equation similar to Eq. A.1 can be defined and solved in a way similar to that proposed by Henry and Pimenta (2018) for hybrid bricks, and the values of γ_k, τ_k and $\Delta\sigma_k$ (defined in Fig. A.1b) can be calculated from γ_{k-1}, τ_{k-1} and $\Delta\sigma_{k-1}$. This allows for the stress-strain responses of each segment to be calculated successively; finally, the stress-strain response of the whole overlap is obtained by combining the response of the 4 segments in series.

This analysis was presented for the particular case of subdomains and segments shown in Fig. A.1, but it can be extended to any generic case using the same methodology as proposed by Henry and Pimenta (2018) for hybrid brick-and-mortar composites.

References

Abaqus. *Abaqus 6.13 Online Documentation, Dassault Systèmes*. Simulia, 2013. URL http://abaqus.cc.ic.ac.uk/v6.13/books/usb/default.htm.

N. Abid, M. Mirkhalaf, and F. Barthelat. Discrete-element modeling of nacre-like materials: Effects of random microstructures on strain localization and mechanical performance. *Journal of the Mechanics and Physics of Solids*, 112:385–402, 2018. ISSN 0022-5096. doi: 10.1016/j.jmps.2017.11.003. URL https://doi.org/10.1016/j.jmps.2017.11.003.

F. Barthelat and R. Rabiei. Toughness amplification in natural composites. *Journal of the Mechanics and Physics of Solids*, 59(4):829–840, 2011. ISSN 00225096. doi: 10.1016/j.jmps.2011.01.001. URL http://dx.doi.org/10.1016/j.jmps.2011.01.001.

F. Barthelat and D. Zhu. A novel biomimetic material duplicating the structure and mechanics of natural nacre. *Journal of Materials Research*, 26(10):1203–1215, 2011. ISSN 0884-2914. doi: 10.1557/jmr.2011.65.

K. Brandt, M. F. H. Wolff, V. Salikov, S. Heinrich, and G. A. Schneider. A novel method for a multi-level hierarchical composite with brick-and-mortar structure. *Scientific Reports*, 3:1–8, 2013. doi: 10.1038/srep02322.

G. Bullegas, S. T. Pinho, and S. Pimenta. Engineering the translaminar fracture behaviour of thin-ply composites. *Composites Science and Technology*, 131: 110–122, 2016. ISSN 0266-3538. doi: 10.1016/j.compscitech.2016.06.002. URL http://dx.doi.org/10.1016/j.compscitech.2016.06.002.

J. D. Currey. Mechanical properties of mother of pearl in tension. *Royal Society publishing*, 196: 443–463, 1977.

G. Dai and L. Mishnaevsky. Fatigue of multiscale composites with secondary nanoplatelet reinforcement: 3D computational analysis. *Composites Science and Technology*, 91: 71–81, 2014. ISSN 0266-3538. doi: 10.1016/j.compscitech.2013.11.024. URL http://dx.doi.org/10.1016/j.compscitech.2013.11.024.

Deben. *Deben UK Ltd., in-situ tensile testing.* 2013. URL http://deben.co.uk/tensile-testing/sem/.

H. Gao. Application of fracture mechanics concepts to hierarchical biomechanics of bone and bone-like materials. *International Journal of Fracture*, 138:101–137, 2006. ISSN 03769429. doi: 10.1007/s10704-006-7156-4.

H. Gao, B. Ji, I. L. Jager, E. Arzt, and P. Fratzl. Materials become insensitive to flaws at nanoscale: lessons from nature. *Proceedings of the National Academy of Sciences of the United States of America*, 100(10):5597–5600, 2003. ISSN 00278424. doi: 10.1073/pnas.0631609100.

L. Gorbatikh, S. V. Lomov, and I. Verpoest. Original mechanism of failure initiation revealed through modelling of naturally occurring microstructures. *Journal of the Mechanics and Physics of Solids*, 58(5):735–750, 2010. ISSN 00225096. doi: 10.1016/j.jmps.2010.02.007. URL http://dx.doi.org/10.1016/j.jmps.2010.02.007.

B. Haghpanah, R. Oftadeh, J. Papadopoulos, and A. Vaziri. Self-similar hierarchical honeycombs. *Proceedings of the Royal Society of London A: Mathematical, Physical and Engineering Sciences*, 469(2156):1–19, 2013. doi: 10.1098/rspa.2013.0022.

J. Henry and S. Pimenta. Modelling hybrid effects on the stiffness of aligned discontinuous composites with hybrid fibre-types. *Composites Science and Technology*, 152:275–289, 2017a.

J. Henry and S. Pimenta. Semi-analytical simulation of aligned discontinuous composites. *Composites Science and Technology*, 144:230–244, 2017b. ISSN 0266-3538. doi: 10.1016/j.compscitech.2017.01.027.

J. Henry and S. Pimenta. Virtual testing framework for hybrid aligned discontinuous composites. *Composites Science and Technology*, 159:259–272, 2018.

iMetrum. *iMetrum LTD - Non Contact Precision Measurement.* Simulia, 2018. URL `https://www.imetrum.com/`.

T. Kanit, S. Forest, I. Galliet, V. Mounoury, and D. Jeulin. Determination of the size of the representative volume element for random composites : statistical and numerical approach. *International Journal of Solids and Structures*, 40:3647–3679, 2003. doi: 10.1016/S0020-7683(03)00143-4.

H. Lei, Z. Zhang, and B. Liu. Effect of fiber arrangement on mechanical properties of short fiber reinforced composites. *Composites Science and Technology*, 72 (4):506–514, 2012. ISSN 02663538. doi: 10.1016/j.compscitech.2011.12.011. URL `http://dx.doi.org/10.1016/j.compscitech.2011.12.011`.

G. Mayer. Rigid Biological Systems as Models for Synthetic Composites. *Science (New York, N.Y.)*, 310:1144–1148, 2005.

R. Menig, M. H. Meyers, M. A. Meyers, and K. S. Vecchio. Quasi-static and dynamic mechanical response of Haliotis Rufescens (Abalone) Shells. *Acta Materialia*, 48:2383–2398, 2000.

S. M. Mirkhalaf and F. Barthelat. A laser-engraved glass duplicating the structure, mechanics and performance of natural nacre. *Bioinspiration & Biomimetics*, 10:1–11, 2015. doi: 10.1088/1748-3190/10/2/026005.

S. M. Mirkhalaf, F. M. A. Pires, and R. Simoes. Determination of the size of the Representative Volume Element (RVE) for the simulation of heterogeneous polymers at finite strains. *Finite Elements in Analysis and Design*, 119:30–44, 2016. ISSN 0168-874X. doi: 10.1016/j.finel.2016.05.004. URL `http://dx.doi.org/10.1016/j.finel.2016.05.004`.

R. Mirzaeifar, L. S. Dimas, Z. Qin, and M. J. Buehler. Defect-Tolerant Bioinspired Hierarchical Composites : Simulation and Experiment. *Acta Biomaterialia*, 1:295–304, 2015. doi: 10.1021/ab500120f.

L. Mishnaevsky. Hierarchical composites: Analysis of damage evolution based on fiber bundle model. *Composites Science and Technology*, 71(4):450–460, 2011. ISSN 0266-3538. doi: 10.1016/j.compscitech.2010.12.017. URL `http://dx.doi.org/10.1016/j.compscitech.2010.12.017`.

F. Narducci and S. T. Pinho. Exploiting nacre-inspired crack deflection mechanisms in CFRP via micro-structural design. *Composites Science and Technology*, 153: 178–189, 2017. ISSN 0266-3538. doi: 10.1016/j.compscitech.2017.08.023. URL `https://doi.org/10.1016/j.compscitech.2017.08.023`.

C. Pelissou, J. Baccou, Y. Monerie, and F. Perales. International Journal of Solids and Structures Determination of the size of the representative volume element for random quasi-brittle composites. *International Journal of Solids and Structures*, 46: 2842–2855, 2009. ISSN 0020-7683. doi: 10.1016/j.ijsolstr.2009.03.015. URL `http://dx.doi.org/10.1016/j.ijsolstr.2009.03.015`.

R. Piat and E. Schnack. Hierarchical material modeling of carbon / carbon composites. *Carbon*, 41:2121–2129, 2003.

S. Pimenta and S. T. Pinho. Hierarchical scaling law for the strength of composite fibre bundles. *Journal of the Mechanics and Physics of Solids*, 61:1337–1356, 2013.

S. Pimenta and S. T. Pinho. An analytical model for the translaminar fracture toughness of fibre composites with stochastic quasi-fractal fracture surfaces. *Journal of the Mechanics and Physics of Solids*, 66:78–102, 2014. ISSN 00225096. doi: 10.1016/j.jmps.2014.02.001.

S. Pimenta and P. Robinson. An analytical shear-lag model for brick-and-mortar composites considering non-linear matrix response and failure. *Composites Science and Technology*, 104:111–124, 2014. ISSN 02663538. doi: 10.1016/j.compscitech.2014.09.001. URL `http://dx.doi.org/10.1016/j.compscitech.2014.09.001`.

P. Pingle, J. Sherwood, and L. Gorbatikh. Properties of rigid-line inclusions as building blocks of naturally occurring composites. *Composites Science and Technology*, 68:2267–2272, 2008. doi: 10.1016/j.compscitech.2008.04.015.

J. Y. Rho, L. Kuhn-Spearing, and P. Zioupos. Mechanical properties and the hierarchical structure of bone. *Medical Engineering and Physics*, 20:92–102, 1998. ISSN 13504533. doi: 10.1016/S1350-4533(98)00007-1.

V. S. Romanov, S. V. Lomov, I. Verpoest, and L. Gorbatikh. Can carbon nanotubes grown on fibers fundamentally change stress distribution in a composite? *Composites Part A: Applied Science and Manufacturing*, 63:32–34, 2014. ISSN 1359835X. doi: 10.1016/j.compositesa.2014.03.021. URL `http://dx.doi.org/10.1016/j.compositesa.2014.03.021`.

Skyflex. *USN020A carbon/epoxy prepreg technical datasheet*. 2015.

X. Wei, T. Filleter, and H. D. Espinosa. Statistical shear lag model – Unraveling the size effect in hierarchical composites. *Acta Biomaterialia*, 18:206–212, 2015. ISSN 1742-7061. doi: 10.1016/j.actbio.2015.01.040. URL `http://dx.doi.org/10.1016/j.actbio.2015.01.040`.

S. Weiner and H. D. Wagner. The material bone: Structure-Mechanical Function Relations. *Annual Review of Materials Research*, 28:271–298, 1998.

W. Xia, J. Song, Z. Meng, C. Shao, and S. Keten. Designing multi-layer graphene-based assemblies for enhanced toughness in nacre-inspired nanocomposites. *Molecular Systems Design & Engineering*, 1:40–47, 2016. ISSN 2058-9689. doi: 10.1039/C6ME00022C. URL `http://dx.doi.org/10.1039/C6ME00022C`.

H. M. Yao and H. J. Gao. Multi-scale cohesive laws in hierarchical materials. *International Journal of Solids and Structures*, 44:8177–8193, 2007. ISSN 00207683. doi: DOI 10.1016/j.ijsolstr.2007.06.007. URL `<Go to ISI>://000251775400006`.

Z. Zhang, Y.-W. Zhang, and H. Gao. On optimal hierarchy of load-bearing biological materials. *Proceedings. Biological sciences / The Royal Society*, 278(September 2010):519–525, 2011. ISSN 0962-8452. doi: 10.1098/rspb.2010.1093.

Z. Q. Zhang, B. Liu, Y. Huang, K. C. Hwang, and H. Gao. Mechanical properties of unidirectional nanocomposites with non-uniformly or randomly staggered platelet distribution. *Journal of the Mechanics and Physics of Solids*, 58(10):1646–1660, 2010. ISSN 0022-5096. doi: 10.1016/j.jmps.2010.07.004. URL `http://dx.doi.org/10.1016/j.jmps.2010.07.004`.